INTERNATIONAL JOURNAL FOR NUMERICAL METHODS IN ENGINEERING
Int. J. Numer. Meth. Engng 2001; **50**:2317–2338

Low-Reynolds-number flow around an oscillating circular cylinder using a cell viscous boundary element method

B. Uzunoğlu[1,2], M. Tan[1,*,†] and W. G. Price[1]

[1] *School of Engineering Sciences, Ship Science, University of Southampton, SO17 1BJ, U.K.*
[2] *Computational Engineering and Design Centre, University of Southampton, U.K.*

SUMMARY

Flow fields from transversely oscillating circular cylinders in water at rest are studied by numerical solutions of the two-dimensional unsteady incompressible Navier–Stokes equations adopting a primitive-variable formulation. These findings are successfully compared with experimental observations. The cell viscous boundary element scheme developed is first validated to examine convergence of solution and the influence of discretization within the numerical scheme of study before the comparisons are undertaken. A hybrid approach utilising boundary element and finite element methods is adopted in the cell viscous boundary element method. That is, cell equations are generated using the principles of a boundary element method with global equations derived following the procedures of finite element methods. The influence of key parameters, i.e. Reynolds number *Re*, Keulegan–Carpenter number KC and Stokes' number β, on overall flow characteristics and vortex shedding mechanisms are investigated through comparisons with experimental findings and theoretical predictions. The latter extends the study into assessment of the values of the drag coefficient, added mass or inertia coefficient with key parameters and the variation of lift and in-line force results with time derived from the Morison's equation. The cell viscous boundary element method as described herein is shown to produce solutions which agree very favourably with experimental observations, measurements and other theoretical findings. Copyright © 2001 John Wiley & Sons, Ltd.

KEY WORDS: hybrid scheme; boundary element method; finite element method; oscillating cylinder; vortex shedding; Navier–Stokes equation

1. INTRODUCTION

Bodies oscillating in a stationary or unsteady fluid flow and stationary bodies in an oscillating unsteady flow are fluid–structure interaction problems of immense practical and theoretical interest in the fields of naval architecture, aerospace, civil and offshore engineering. For example, a ship or aircraft manoeuvring, a submersible oscillating under prescribed experimental

---

[*] Correspondence to: Mingyi Tan, School of Engineering Sciences, Ship Science, University of Southampton, Highfield, Southampton, SO17 1BJ; U.K.
[†] E-mail: mingyi@ship.soton.ac.uk

Received 16 December 1999
Revised 9 May 2000

conditions to measure fluid actions, cylindrical tubular structures (i.e. offshore platforms, risers, etc.) subject to current and wave loads, bodies (i.e. bridges, chimneys, etc.) experiencing steady or wind gust loads, etc. are practical illustrations of fluid–structure interactions, facets of which are discussed by Duncan [1], Burcher [2], Etkin [3], Sarpkaya and Isaacson [4] and Faltinsen [5].

In offshore engineering, in particular, bluff bodies in the form of cylinders are extensively used in construction and, in many ways, they form the cornerstone of developments in oil extraction from beneath the sea. For such reasons, the interaction between viscous fluid flows and circular cylinders is of significant importance stimulating extensive experimental and theoretical investigations. These aim to understand the underlying complex physical interaction mechanisms, to simulate the behaviour and characteristics of the fluid flow within the interaction process and to model mathematically the fluid actions experienced by circular cylinders. Sarpkaya and Isaacson [4], Faltinsen [5] and Baltrop and Adams [6] provide extensive overviews of such studies.

The flow past a circular cylinder fixed in a steady stream, the flow experienced by a circular cylinder in an oscillating flow or the flow generated by an oscillating cylinder in a stationary or unsteady flow are fluid–structure interaction problems investigated both experimentally and theoretically. They provide information through observation, measurement and predictions of the strengths, trajectories and frequencies of generated vortices, the magnitudes of the fluid actions through lift forces, drag forces, moments and their associated added mass, added inertia and drag coefficients, etc. Such related information is presented experimentally by Hassan [7], Bishop and Hassan [8], Maull and Milliner [9], Bearman [10], Williamson [11, 12], Obasaju *et al.* [13] and Tatsuno and Bearman [14]. As an example, the latter investigators examined the viscous fluid flow characteristics around a circular cylinder of diameter D oscillating transversely with amplitude A, frequency ω and with a translational motion

$$\begin{aligned} x(t) &= -A\sin(2\pi f t) = -A\sin(\omega t) \\ \dot{x}(t) &= -A\omega\cos(\omega t) = -U_m\cos(\omega t) \end{aligned} \tag{1}$$

Their experimental findings clearly illustrate the complexity of the vortex patterns generated which were classified on the basis of the following parameters:

$$\begin{aligned} &\text{Keulegan–Carpenter number} \quad \mathrm{KC} = \frac{U_m T}{D} = \frac{(\omega A)(2\pi/\omega)}{D} = \frac{2\pi A}{D} \\ &\text{Stokes' parameter} \quad \beta = \frac{\rho D^2}{\mu T} \\ &\text{Reynolds number } Re = \mathrm{KC} \quad \beta = \frac{\rho\omega A D}{\mu} = \frac{\rho U_m D}{\mu} \end{aligned} \tag{2}$$

where μ represents the coefficient of viscosity and ρ denotes the fluid density. Figure 1 illustrates the dependence of the various flow regimes on Keulegan–Carpenter number and Reynolds number or Stokes' parameter as observed by Tatsuno and Bearman [14].

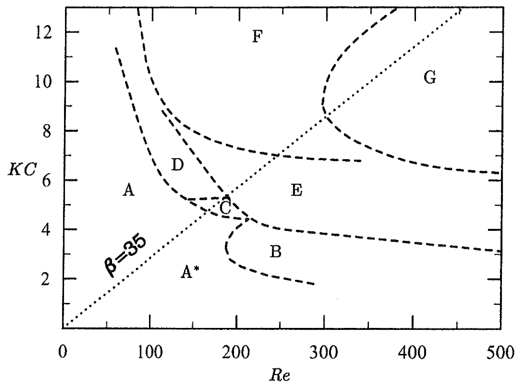

Figure 1. Flow regimes defined by Tatsuno and Bearman [14] and also Dütsch *et al.* [15]. The principal features of the regions are: (A*) No flow separation, secondary streaming, two dimensional; (A) two vortices shed symmetrically per half cycle, two dimensional; (B) three-dimensional instability, longitudinal vortices; (C) rearrangement of large vortices, three dimensional; (D) flow convected obliquely to one side of the axis of oscillation, three dimensional; (E) irregular switching of flow convection direction, three dimensional; (F) flow convected diagonally, three dimensional; (G) transverse vortex street, three dimensional.

To complement such experimental investigations, several numerical studies of the unsteady flow around a circular cylinder at low KC values have been presented by, for example, Dütsch *et al.* [15], Borthwick [16], Smith and Stansby [17], Justesen [18], Wang and Dalton [19], Lin *et al.* [20] and Zhang and Zhang [21].

To model mathematically the unsteady oscillatory force acting on a cylinder, Morison *et al.* [22] developed a semi-empirical formulation which has since been extensively used in offshore engineering. This approach is discussed by Sarpkaya and Isaacson [23] who for an oscillating cylinder in a stationary fluid expressed the force per unit length in the form,

$$F_1(t) = -\tfrac{1}{2}\rho D C_D \dot{x}|\dot{x}| - \tfrac{1}{4}\rho\pi D^2 C_I \ddot{x} \tag{3}$$

whereas, for a stationary cylinder in an oscillating fluid the equation is given by

$$F_1(t) = -\tfrac{1}{2}\rho D C_D \dot{x}|\dot{x}| - \tfrac{1}{4}\rho\pi D^2 C_M \ddot{x} \tag{4}$$

where $C_M = C_I + 1$. Here C_I, C_M and C_D denote the added mass, added inertia and drag coefficients, respectively, and the difference between C_M and C_I arises because of the change in the defining co-ordinate system used to describe the fluid–structure dynamics. These coefficients are determined from experiments or from numerical solutions of the Navier–Stokes equations. Estimates of their values can be determined using a variety of analysis techniques and methods (i.e. Fourier, least-squares, etc.) as discussed by Sarpkaya [23] and Sarpkaya and Isaacson [4].

Stokes [24] first determined analytical expressions for the C_D and C_M coefficients provided that the cylinder flow remains attached, laminar and two dimensional. It was shown that the forces acting on a sinusoidally oscillating cylinder depend on both KC, *Re* or β and in an extension of Stokes' theoretical approach, Wang [25] derived the following expressions:

$$C_D = \frac{3\pi^3}{2\mathrm{KC}}\left[(\pi\beta)^{-1/2} + (\pi\beta)^{-1} - \frac{1}{4}(\pi\beta)^{-3/2}\right] \tag{5}$$

$$C_M = 2 + 4(\pi\beta)^{-1/2} + (\pi\beta)^{-3/2} \tag{6}$$

for $Re\,\mathrm{KC} \ll 1$ and $\beta \gg 1$. The first two terms in these formulae replicate Stokes' findings.

The values of these theoretical coefficients agree favourably with experimental findings for two-dimensional flows as discussed by Lin *et al.* [20]. However, as illustrated in Figure 1, such flow regimes are limited and as the KC value increases complex three-dimensional vortex patterns are generated. Honji [26] observed experimentally, and confirmed theoretically by Hall [27], a three-dimensional instability on the attached boundary of the cylinder generating counter rotating vortex structures along the cylinder's span. This effect causes an increase in the predicted coefficient values of Wang as confirmed by Sarpkaya [28] in a comparative analysis of theoretical findings (based on the Stokes' and Wang models) and experimental investigations into the influence of KC value on the occurrence of the Honji instability. Hall [27] deduced that this occurs at the critical Keulegan–Carpenter number defined by

$$K_{\mathrm{cr}} = \frac{Re_{\mathrm{cr}}}{\beta} = 5.778\beta^{-1/4}(1 + 0.205\beta^{-1/4} + \cdots) \tag{7}$$

In this present study, the flow characteristics and C_D and C_M coefficient values associated with a stationary circular cylinder in an oscillating viscous flow and an oscillating cylinder in a stationary fluid are investigated using the cell boundary element method developed by Tan *et al.* [29]. This hybrid approach incorporates both boundary element and finite element methods since, in the proposed scheme of study, cell equations based on Navier–Stokes equations are generated using the principles of the boundary element method with global equations applicable over the whole fluid domain derived following the procedures of the finite element method. A primitive-variable formulation with an unstructured fluid domain mesh requirement forms the basis of the hybrid approach. This can be applied to both two- and three-dimensional problems associated with a single cylinder or arbitrary arrangements of circular cylinders or other shaped bodies as discussed by Farrant *et al.* [30, 31]. The application of the proposed method focuses on two-dimensional fluid–structure interactions incorporating a validation with experimental vortex shedding flows observed and measured by Tatsuno and Bearman [14], Kühtz [32] and a comparison of predictions derived by Dütsch *et al.* [15] by a finite volume method.

2. MATHEMATICAL THEORY

2.1. Governing equations

Figure 2 illustrates a cell idealization of the viscous fluid domain. In each typical cell or element Ω, bounded by surface Σ, the fluid is assumed incompressible and of constant viscosity. The Navier–Stokes equations describing the flow velocity $\mathbf{v}'(\mathbf{x}', t')$ and the mean pressure

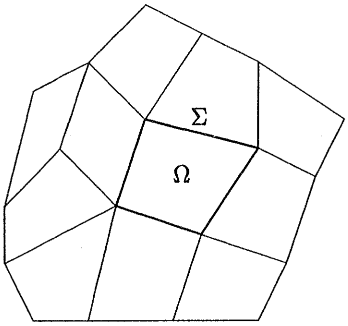

Figure 2. Discretization of the fluid domain by an unstructured mesh.

$p'(\mathbf{x}',t')$ of the viscous fluid are given by

$$\frac{\partial v'_j}{\partial t'} + (v'_j v'_k)_{,k'} + \frac{1}{\rho'} p'_{,j'} - \frac{1}{\rho'}[\mu'(v'_{j,k'} + v'_{k,j'})]_{,k'} = 0 \tag{8}$$

$$v'_{j,j'} = 0 \tag{9}$$

Here ρ' and μ' represent the fluid density and viscosity. A prime ($'$) indicates the variable is a dimensional quantity.

In order to simplify the mathematical expressions in these equations, a tensor index notation with summation convention is adopted. In the convective term, for example,

$$(v'_j v'_k)_{,k'} = \sum_{k=1} \frac{\partial (v'_j v'_k)}{\partial x'_k}$$

where the upper limit of the summation takes the value 2 or 3 for two-dimensional or three-dimensional problems, respectively.

For viscous fluid–structure interaction problems categorized by a characteristic length L' (e.g. diameter of cylinder, say) and a characteristic velocity U' (e.g. mean fluid velocity), the non-dimensional variables of space $\mathbf{x}$, time t, velocity $\mathbf{v}$ and pressure p are defined by

$$\mathbf{x} = \frac{\mathbf{x}'}{L'}, \quad t = \frac{U'}{L'} t', \quad \mathbf{v} = \frac{\mathbf{v}'}{U'}, \quad p = \frac{p'}{\rho' U'^2}$$

such that (8) and (9) can be expressed in the dimensionless forms:

$$\dot{v}_j + (v_j v_k)_{,k} + p_{,j} - [\nu_e (v_{j,k} + v_{k,j})]_{,k} = 0 \tag{10}$$

$$v_{j,j} = 0 \tag{11}$$

Here $\nu_e = 1/Re$ where Re denotes the Reynolds number ($= \rho' U' L'/\mu'$).

These equations represent the flow velocity in an inertial or space fixed frame of reference and are appropriate to the analysis of the fluid–structure interaction between a fixed body and an oscillating flow. For a body manoeuvring in an incompressible fluid, Price and Tan [33] showed that the Navier–Stokes equations formulated in a moving frame of reference attached to the body are given by

$$\dot{v}_j + (v_j U_k)_{,k} + p_{,j} - [v_e(v_{j,k} + v_{k,j})]_{,k} = 0 \tag{12}$$

$$v_{j,j} = 0 \tag{13}$$

Here U_k denotes the relative velocity between the body and the fluid motion, i.e. $U_k = v_k - \hat{v}_k$ where $\hat{v}_k$ represents the velocity of the body and/or the fluid mesh attached to the body. This set of equations is suitable to describe the fluid–structure interaction between a cylinder oscillating horizontally and a fluid at rest at infinity or pulsating and translating in a stationary fluid. As can be seen, these two sets of equations are very similar to (10) derived by setting $\hat{v}_k = 0$ in (12). Therefore, for generality, (12) and (13) are used in the following development of the mathematical model and numerical scheme of study.

2.2. *Integral equation*

To improve the efficiency and effectiveness of the numerical scheme of study for time-dependent unsteady flow problems, the non-linear convective term in the momentum equation is first resolved by a time marching process before the Navier–Stokes equations are transformed into an integral equation (see Reference [29]). The procedure is described as follows:

(1) *First-order scheme*
In this scheme, the non-linear convective term can be resolved by a time-stepping process. To maintain an accuracy of the order of Δt in the solution, the equation at the $(n+1)$th time step takes the form

$$f_j + (v_j \tilde{U}_k)_{,k} + p_{,j} - [v_e(v_{j,k} + v_{k,j})]_{,k} = 0$$

where $f_j = (1/\Delta t)[v_j - v_j^{(n)}]$, $\tilde{U}_k = v_k^{(n)} - \hat{v}_k$ denotes the relative velocity at the nth time step and the $\hat{v}_k$ represents the corresponding body velocity. Little additional computational time is needed to transform the velocity vector field into a space fixed co-ordinate system by adding the system velocities.

(2) *Second-order scheme*
To achieve a second-order level of numerical accuracy with respect to Δt, the equation for the $(n+1)$th time step is similar to the first-order scheme except in this case,

$$f_j = (1/2\Delta t)[3v_j - 4v_j^{(n)} + v_j^{(n-1)}] \quad \text{and} \quad \tilde{U}_k = 2v_k^{(n)} - v_k^{(n-1)} - \hat{v}_k$$

The mathematical theory for the derivation of above formulations can be found in Reference [34].

Thus, with the appropriate definitions of f_j and $\tilde{U}_k$, these previous schemes can be represented by the modified Navier–Stokes equation,

$$f_j + (v_j \tilde{U}_k)_{,k} + p_{,j} - [v_e(v_{j,k} + v_{k,j})]_{,k} = 0 \tag{14}$$

By means of Gauss's theorem, an integral equality involving functions $\mathbf{v}, p$ and two additional functions $\mathbf{v}_s^*$ and p_s^* can be established on a typical cell Ω bounded by its surface

Σ with outward normal $\mathbf{n}$ (see Reference [35]). This is written as

$$\begin{aligned}
&\int_\Omega \{v^*_{sj}[f_j + (v_j\tilde{U}_k)_{,k} + p_{,j} - (\nu_e(v_{j,k} + v_{k,j}))_{,k}] + p^*_s v_{j,j}\}\,\mathrm{d}\Omega \\
&\quad + \int_\Omega \{v_j[\tilde{U}_k v^*_{sj,k} + p^*_{s,j} + (\nu_e(v^*_{sj,k} + v^*_{sk,j}))_{,k}] + p v^*_{sj,j}\}\,\mathrm{d}\Omega \\
&\quad = \int_\Sigma [v_j(\tilde{U}_k n_k v^*_{sj} + R^*_{sj}) - R_j v^*_{sj}]\,\mathrm{d}\Sigma + \int_\Omega f_j v^*_{sj}\,\mathrm{d}\Omega
\end{aligned} \tag{15}$$

where the term $R_j = -pn_j + \nu_e(v_{j,k} + v_{k,j})n_k$ represents the jth component of the dimensionless traction on the surface Σ whereas the variable R^*_{sj} is defined as

$$R^*_{sj} = p^*_s n_j + \nu_e(v^*_{sj,k} + v^*_{sk,j})n_k$$

This integral equality holds for any functions $\mathbf{v}, p, \mathbf{v}^*_s$ and p^*_s provided that all the terms involved are integrable. If functions $\mathbf{v}$ and p are reserved to represent the flow velocity and the mean pressure in the fluid on the cell, respectively, and they satisfy (11) and (14) then the forms of functions $\mathbf{v}^*_s$ and p^*_s can be selected by imposing appropriate conditions to simplify (15). In fact an examination of the integral equality shows that there would be significant mathematical simplification by letting $\mathbf{v}^*_s$ and p^*_s satisfy the following equations:

$$\tilde{U}_k v^*_{sj,k} + p^*_{s,j} + (\nu_e(v^*_{sj,k} + v^*_{sk,j}))_{,k} = -\delta_{sj}\Delta(\mathbf{x} - \boldsymbol{\xi}) \tag{16}$$

$$v^*_{sj,j} = 0 \tag{17}$$

where δ_{sj} and $\Delta(\ )$ are Kronecker and Dirac delta functions, respectively.

With the functions $\mathbf{v}^*_s$ and p^*_s defined by these equations, (15) reduces to,

$$C(\boldsymbol{\xi})v_s(\boldsymbol{\xi}, t) + \int_\Sigma v_j(\tilde{\mathbf{U}}\cdot\mathbf{n}v^*_{sj} + R^*_{sj})\,\mathrm{d}\Sigma = \int_\Sigma R_j v^*_{sj}\,\mathrm{d}\Sigma - \int_\Omega f_j v^*_{sj}\,\mathrm{d}\Omega \tag{18}$$

where

$$C(\boldsymbol{\xi}) = \begin{cases} 1 & \text{if } \boldsymbol{\xi} \in \Omega \\ \frac{1}{2} & \text{if } \boldsymbol{\xi} \in \Sigma \\ 0 & \text{otherwise} \end{cases}$$

In this equation the velocity of the flow in the cell is expressed as a surface integral of velocity and traction on the boundary, and an additional volume integral involving the contribution from f_j which can be calculated from the values of v_j and $\mathbf{v}^{(n)}$ on the cell boundary.

When the boundary values of the velocity are specified, (18) can be used to determine the traction $\mathbf{R}$ on the boundary and then the velocity field $\mathbf{v}$ everywhere in the cell. Thus (18) defines a relation between the velocity and force on the cell boundary. Since v^*_{sj} also depends on the value of $\tilde{\mathbf{U}}$ in the cell as seen from (16), modifications to the values of v^*_{sj} are needed during the time stepping procedures as $\mathbf{v}$ is continuously updated in the computation.

2.3. *Fundamental solution*

In the context of this paper, the solution of (16) and (17) is referred to as the fundamental solution of the problem as it describes the response of the system to a point excitation. To simplify the process of solution of these two equations for v_{sj}^* and p_s^*, a further approximation is introduced to replace the convective velocity $\tilde{\mathbf{U}}$ (with component $\tilde{U}_k$) in (16) by its mean value $\mathbf{u}$ (with component u_k) on the cell. Findings from numerical experiments reveal that this approximation is superior to the first-order approximation, in which the value of $\tilde{U}_k$ at any arbitrary point in the cell is used for the convective velocity in (16).

With this assumption, the equations defining v_{sj}^* and p_s^* take the following form:

$$u_k v_{sj,k}^* + p_{s,j}^* + (v_e(v_{sj,k}^* + v_{sk,j}^*))_{,k} = -\delta_{sj}\Delta(\mathbf{x} - \xi) \tag{19}$$

$$v_{sj,j}^* = 0 \tag{20}$$

The solutions of these equations for both two- and three-dimensional cases can be obtained by means of Fourier transformations as discussed by Price and Tan [36, 33], or Tan [35].

3. NUMERICAL MODELLING

3.1. *Idealization*

To provide solutions to unsteady fluid–structure interaction problems, the computational fluid domain is discretized into a large number of cells or elements (see Figure 2) and the integral (18) adopted to represent the velocity field on the cell in terms of the values of velocity and traction on the cell boundary.

For simplicity the following discussions are restricted to the two-dimensional time-dependent case involving only quadrilateral cells with the control points for the unknown functions taken at the centre of each cell edge. Similar discussions, however, apply to more general cases, i.e. three-dimensional problems, control points taken at the corners of each quadrilateral, control points at centres and corner points, etc.

3.2. *Cell equations*

On the typical cell shown in Figure 3, if the first-order time-stepping scheme is assumed and the unknown functions $\mathbf{v}$ and $\mathbf{R}$ on each edge are treated as constants taking their values at the centre of each edge, the cell integral equation can be rewritten as

$$\begin{aligned} C(\xi)v_s(\xi,t) + \sum_{l=1}^{4} v_j^{(l)} \int_{(l)} (\mathbf{u}\cdot\mathbf{n}v_{sj}^* + R_{sj}^*)\,\mathrm{d}\Sigma + \frac{1}{\Delta t}\int_\Omega v_j v_{sj}^*\,\mathrm{d}\Omega \\ = \sum_{l=1}^{4} R_j^{(l)} \int_{(l)} v_{sj}^*\,\mathrm{d}\Sigma + \frac{1}{\Delta t}\int_\Omega v_j^{(n)} v_{sj}^*\,\mathrm{d}\Omega \end{aligned} \tag{21}$$

When the co-ordinates of the control point on each edge are assigned successively to ξ, the index s allowed to take values 1 and 2 for the two-dimensional case under examination and

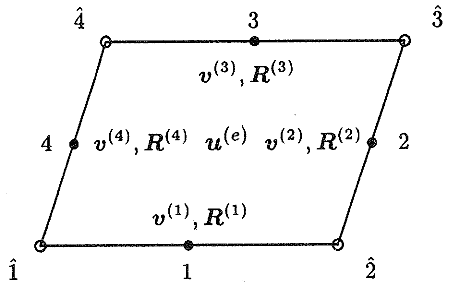

Figure 3. A typical cell with ordered notation.

the integrations of v_{sj}^* and R_{sj}^* completed, the integral equation is replaced by a discretization involving a set of 8 simultaneous equations on each cell. Thus if the superscript e denotes the eth cell then the relevant algebraic equations can be expressed in the form

$$A_{\mathrm{v}}^{(e)} V^{(e)} = A_{\mathrm{r}}^{(e)} R^{(e)} + b^{(e)} \tag{22}$$

Here $V^{(e)}$ and $R^{(e)}$ are single column arrays constructed from the velocity $\mathbf{v}^{(l)}$ and traction $\mathbf{R}^{(l)}$ values at the centre of each edge $(l = 1, 2, 3, 4)$ on the cell boundary. That is

$$V^{(e)} = \begin{Bmatrix} \mathbf{v}^{(1)} \\ \mathbf{v}^{(2)} \\ \mathbf{v}^{(3)} \\ \mathbf{v}^{(4)} \end{Bmatrix}, \quad R^{(e)} = \begin{Bmatrix} \mathbf{R}^{(1)} \\ \mathbf{R}^{(2)} \\ \mathbf{R}^{(3)} \\ \mathbf{R}^{(4)} \end{Bmatrix}$$

where $A_{\mathrm{v}}^{(e)}$ and $A_{\mathrm{r}}^{(e)}$ are 8×8 matrices and $b^{(e)}$ a vector with 8 elements. These terms are the results of the integration of v_{sj}^* and R_{sj}^* on the cell and can be expressed formally as

$$A_{\mathrm{v}}^{(e)} = \left[\frac{1}{2} \delta_{sj} + \int_{(l)} (\mathbf{u} \cdot \mathbf{n} v_{sj}^* + R_{sj}^*) \, \mathrm{d}\Sigma + \frac{1}{4\Delta t} \int_{\Omega} v_{sj}^* \, \mathrm{d}\Omega \right] \tag{23}$$

$$A_{\mathrm{r}}^{(e)} = \left[\int_{(l)} v_{sj}^* \, \mathrm{d}\Sigma \right], \quad b^{(e)} = \left\{ \frac{\bar{v}_j^{(n)}}{\Delta t} \int_{\Omega} v_{sj}^* \, \mathrm{d}\Omega \right\} \tag{24}$$

where $\bar{v}_j^{(n)}$ is the averaged velocity of the nth time step on the cell and only the contribution from the mean acceleration on the cell is included in the equations.

From (22), an expression of $R^{(e)}$ can be obtained in the form

$$R^{(e)} = C^{(e)} V^{(e)} - d^{(e)} \tag{25}$$

where $C^{(e)}$ and $d^{(e)}$ are solutions of the equations

$$A_{\mathrm{r}}^{(e)} C^{(e)} = A_{\mathrm{v}}^{(e)}, \quad A_{\mathrm{r}}^{(e)} d^{(e)} = b^{(e)}$$

In this formulation, the matrix $A_r^{(e)}$ is nearly singular because the flow is incompressible. The singular value decomposition method (see [37, Section 2.9]) can be adopted to solve these equations to find $C^{(e)}$ and $d^{(e)}$.

3.3. Global equations

The action–reaction relation of the traction **R** and the continuity of the velocity field **V** across the control point on the cell boundary require **R** and **V** to satisfy the expressions

$$\mathbf{R}^{(l)} + \mathbf{R}'^{(l')} = \mathbf{0}, \quad \mathbf{V}^{(l)} = \mathbf{V}'^{(l')} \tag{26}$$

Here $\mathbf{R}^{(l)}, \mathbf{R}'^{(l')}, \mathbf{V}^{(l)}$ and $\mathbf{V}'^{(l')}$ are the values of the traction and velocity on the same control point belonging to different cells.

To construct the global equations for the whole fluid domain from the cell equations, the assembly process used in a finite element method to obtain the stiffness matrix is adopted [38, Sections 1.3 – 1.7]. The control points are organized into a consecutive global order after each point is given a unique control point identifying number. When conditions (26) are applied to each control point and the contributions from all cell equations to each and every control point collected, a set of algebraic equations in terms of velocity can be obtained for the whole computational domain. That is,

$$DV = F \tag{27}$$

where V is the array of velocity values on all the control points in the global order, F contains the contributions of $b^{(e)}$ from all cells and D is formed by assembling the cell matrix $C^{(e)}$ according to the global order of each control point.

Before this set of equations can be solved, global boundary conditions need to be implemented. The two most commonly encountered conditions are prescribed traction and prescribed velocity on the boundary.

4. NUMERICAL RESULTS

4.1. Discretization parameters and convergence

In this study, a selection of viscous flow characteristics, predicted by the cell boundary mathematical model, is compared with observations, measurements and other relevant theoretical findings. Such an exercise provides a measure of verification and validation of the proposed approach and developed numerical scheme of study; it also provides a degree of confidence to extend the theoretical model to tackle more complex unsteady fluid–structure interaction problems as considered by Farrant *et al.* [31].

Figure 4 illustrates the flow domain surrounding a circular cylinder of non-dimensional unit diameter. The overall size of the discretized fluid domain adopted in the calculations is defined by the magnitude of the quantity denoted by h (i.e. $h = 3, 6, 9$, etc.). Figure 5 shows a typical unstructured mesh of the fluid domain with each rectangular cell of grid size $(\Delta x, \Delta y)$, where $\Delta x, \Delta y$ denote horizontal and vertical dimensions, respectively. In a study to assess the influence of the domain size, grid dimension and idealization two different sets of boundary conditions were assumed, each associated with a particular fluid problem. In Figure 4, the

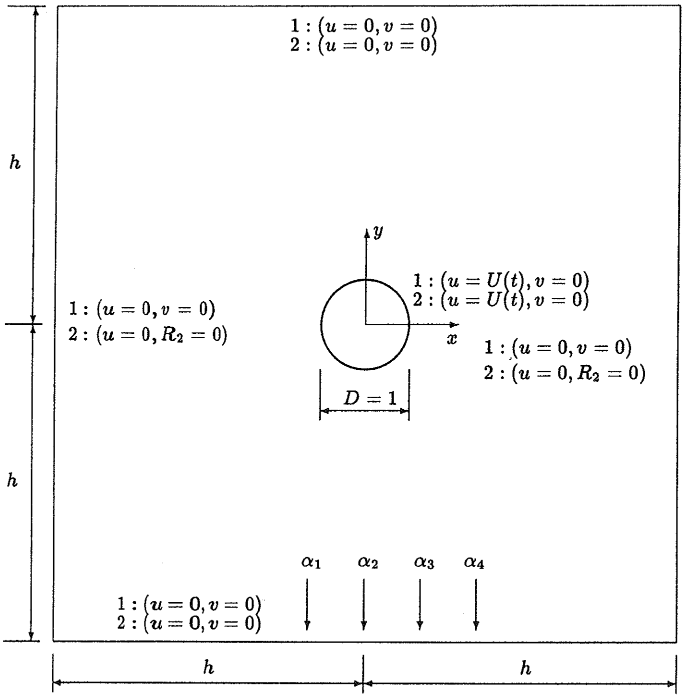

Figure 4. Computational domain definition and boundary conditions for an oscillating cylinder. All the variables and quantities are non-dimensional. (The indicated positions $\alpha_1, \alpha_2, \alpha_3, \alpha_4$ relate to the transverse measurements of Dütsch *et al.* [15] illustrated in Figure 10.)

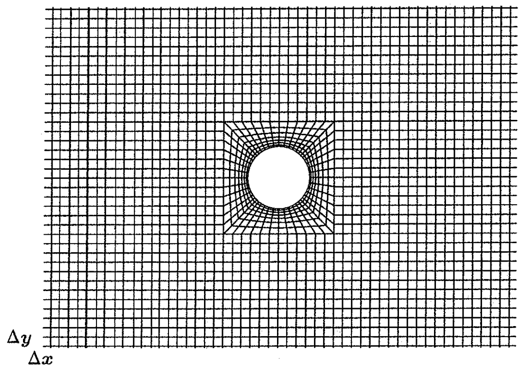

Figure 5. Typical mesh idealizing the fluid around the cylinder.

boundary conditions (1) and (2) refer to a transversely oscillating cylinder with the far-field fluid at rest. At the top and the bottom of the domain the same velocity boundary conditions are assumed. By slight modification of these conditions a numerical towing tank experiment in which the cylinder translates with a forward speed $v = V(t)$ and transversely oscillates with prescribed motion $u = U(t)$ as given in (1) can be devised.

Table I. Drag C_D and added mass C_I coefficients at $Re = 100$ and $KC = 5$ for different time steps.

Δt	Boundary condition (Figure 4)	Domain size h	Grid size $(\Delta x, \Delta y)$	C_D	C_I
0.25000	1	6.0	(0.15, 0.15)	1.98	1.48
0.12500	1	6.0	(0.15, 0.15)	2.09	1.44
0.06250	1	6.0	(0.15, 0.15)	2.10	1.43
0.03125	1	6.0	(0.15, 0.15)	2.10	1.43

Table II. Drag C_D and added mass C_I coefficients at $Re = 100$ and $KC = 5$ for different boundary conditions and domain size.

Δt	Boundary condition (Figure 4)	Domain size h	Grid size $(\Delta x, \Delta y)$	C_D	C_I
0.06250	1	3.0	(0.15, 0.15)	2.27	1.47
0.06250	2	3.0	(0.15, 0.15)	2.24	1.49
0.06250	1	6.0	(0.15, 0.15)	2.10	1.43
0.06250	2	6.0	(0.15, 0.15)	2.13	1.44
0.06250	1	9.0	(0.15, 0.15)	2.10	1.43
0.06250	2	9.0	(0.15, 0.15)	2.10	1.43

Table III. Drag C_D and added mass C_I coefficients at $Re = 100$ and $KC = 5$ for meshes of different refinement.

Δt	Boundary condition (Figure 4)	Domain size h	Grid size $(\Delta x, \Delta y)$	C_D	C_I
0.06250	1	6.0	(0.20, 0.20)	2.12	1.41
0.06250	1	6.0	(0.15, 0.15)	2.10	1.43
0.06250	1	6.0	(0.10, 0.10)	2.10	1.45
	Finite volume method, Dütsch *et al.* [15]*			2.09	1.45

*Numerical results derived using the finest mesh in their analysis.

For the fluid flow at $Re = 100$, $KC = 5$, designated two-dimensional by Tatsuno and Bearman [14] in Figure 1, Tables 1–3 show the variations of the values of the drag coefficient C_D and added mass coefficient C_I with time step Δt, domain size h, grid size $(\Delta x, \Delta y)$ and boundary conditions. Overall the computed C_D, C_I results show small variations between themselves even for significant changes to the stated parameter values. To examine the sensitivity of inlet–outlet boundary condition at $x = \pm h$, Table II includes predictions for velocity boundary conditions, i.e. $u = 0 = v$ and a mixed boundary condition involving velocity and traction components, i.e. $u = 0 = R_2$. From the evidence presented in Table II, it is observed that provided h is sufficiently large the boundary conditions imposed at $x = \pm h$ influence C_D and C_I values insignificantly. In all these findings a larger variation of value is exhibited in the drag coefficient rather than the added mass coefficient which remains relatively constant.

In a wide ranging computational investigation, additional results were further substantiated. Namely, boundary conditions (1) and (2) produce similar predictions for each set of chosen

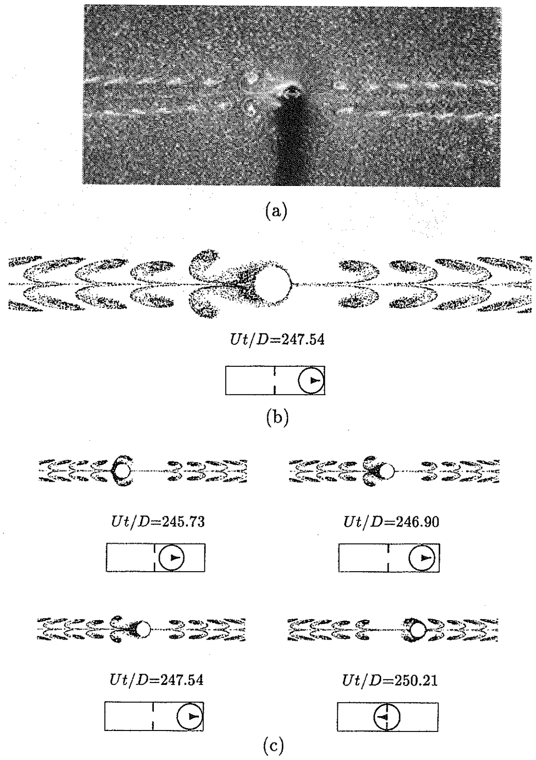

Figure 6. (a) Flow visualization of the streakline pattern generated by a transversely oscillating circular cylinder at $Re = 81.4$, $\mathrm{KC} = 11.0$ in two-dimensional flow regime A as observed by Tatsuno and Bearman [14]; (b) overall numerical simulation comparable with the visualization in (a); (c) numerical simulation at different stages over a half-cycle illustrating the vortex shedding mechanism.

parameter values and, secondly, the observed flow characteristics associated with a cylinder oscillating in a stationary fluid and those for a stationary cylinder subject to an oscillating flow showed very close agreement confirming the study of Garrison [39]. Such studies provide assurance that the numerical schemes of study produce convergent results and this is further confirmed by the finite volume investigation of Dütsch *et al.* [15] who determined drag and added mass coefficient values of $C_D = 2.09$ and $C_I = 1.45$, for $Re = 100$ and $\mathrm{KC} = 5$. These latter values were obtained using the finest mesh in their analysis and they lie within the range of data shown in Tables I–III. It is interesting to note that although favourable comparisons of predicted results are demonstrated between the cell boundary element approach and the finite volume method, the computational domain used herein is smaller and incorporates a coarser mesh than used by Dütsch *et al.* [15].

Thus, from the presented evidence on accuracy of computation and convergence of solution, in subsequent calculations for transversely oscillating cylinders, it was decided to take the following grid dimensions: $\Delta x = 0.15 = \Delta y$; to discretize the fluid domain $h = 9$ for symmetric flow regimes (i.e. see Figures 6 and 7) and $h = 15$ for asymmetrical flows (i.e. C, E, F in Figure 1) to capture details of the more complex flow behaviours (see Figure 8); to utilize

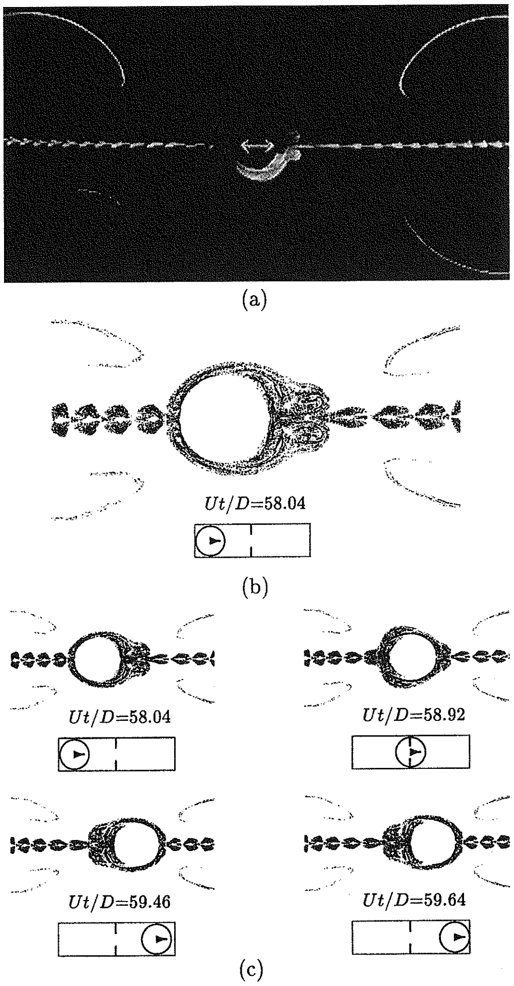

Figure 7. (a) Flow visualization of the streakline pattern generated by a transversely oscillating circular cylinder at $Re = 165.79$, $KC = 3.14$ in two-dimensional flow regime A* as observed by Tatsuno and Bearman [14]; (b) overall numerical simulation comparable with the visualization in (a); (c) numerical simulation at different stages over a half-cycle illustrating the contra-rotating crescent like flow observed.

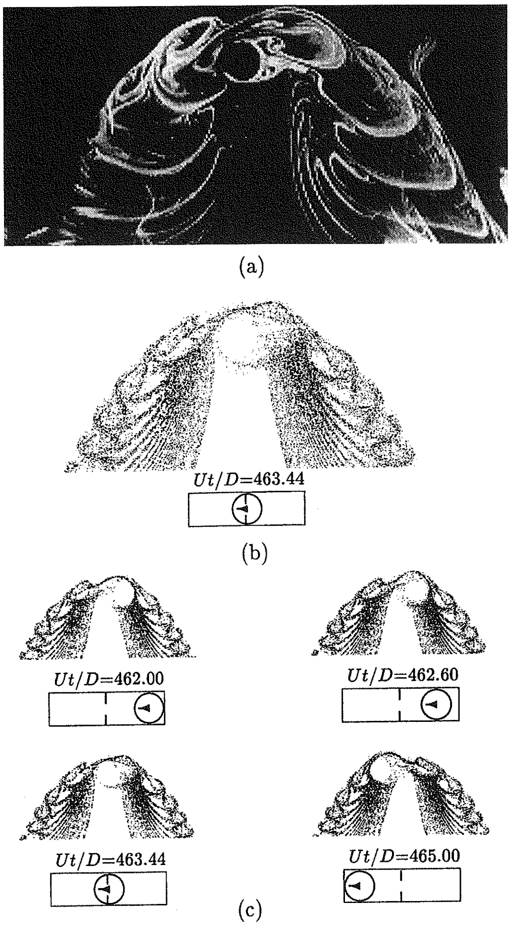

Figure 8. (a) Flow visualization of the streakline pattern generated by a transversely oscillating circular cylinder at $Re = 210.0$, $KC = 6.0$ in three-dimensional flow regime E as observed by Tatsuno and Bearman [14]; (b) overall two-dimensional numerical simulation comparable with the visualization of three-dimensional flow in (a); (c) numerical simulation at different stages over a half-cycle of a stable V-type vortex street which is sharper than observed in (a) due to the confinement of the two-dimensional flow.

a uniform unstructured mesh (see Figure 5); to adopt approximately 80 time steps per cycle and velocity boundary condition (1). That is, the mathematical modelling of the experiments performed by Tatsuno and Bearman [14], Knörnschild [40] and Dütsch *et al.* [15].

The results for the convergence tests of the present method in the oscillating cylinder flow problems are consistent with similar tests carried out for other flow problems including driven cavity flow, backfacing step channel flow and vortex shedding flows, etc. The details of these investigations and more comparison with other methods can be found in Tan *et al.* [29] and Farrant *et al.* [30, 31].

4.2. *Observations and numerical simulations*

As illustrated in Figure 1, Tatsuno and Bearman [14] through an experimental visualization study provide an extensive categorization of the flow regimes around an oscillating circular cylinder over a range of Re and KC numbers. Three such examples are shown in Figures 6(a)–8(a) of the streakline patterns at $Re=81.4$, $\mathrm{KC}=11.0$ in regime A, $Re=165.79$, $\mathrm{KC}=3.14$ in regime A* and $Re=210.0$ and $\mathrm{KC}=6.0$ in regime E. They confirmed the first two flow fields as two-dimensional and these cases are on either side of the $\beta=35$ line shown in Figure 1. Knörnschild [40] independently substantiated these findings. Case E is on the $\beta=35$ line and is deemed a physical three-dimensional flow (see Figure 1).

Figures 6(b)–8(b) illustrate the equivalent computed streakline patterns to Figures 6(a)–8(a). These streaklines were simulated by releasing 40 massless particles at each time step into the computational domain. The overall impression gained by comparison of the respective figures indicates close similarities. The particles used to compute the streakline patterns are passive markers. This method is equivalent to the experimental electrolytic precipitation method used by Tatsuno and Bearman [14].

Figures 6(c)–8(c), 9(a) and 9(c) illustrate the vortex shedding mechanisms in the numerical simulations during various stages of the cycle for cases A, A* and E.

Figures 6(b), 6(c) and 9(a) show symmetric and periodic vortex shedding. In this regime two contra-rotating vortices are formed symmetrically behind the cylinder during each half-cycle. These vortices stay behind the cylinder at the end of each cycle and as the cylinder reverses direction, the vortices are convected towards the cylinder. The vortices do not survive into the next half-cycle agreeing with the observations of Tatsuno and Bearman [14].

Figure 7(b) and 7(c) illustrate computed streakline patterns during a cycle for case A* i.e. $Re=165.79$, $\mathrm{KC}=3.14$. The computed velocity field for this regime at a specific instant in the cycle is illustrated in Figure 9(b). No vortex shedding occurs in this symmetric regime confirming the experimental findings. Large regions of contra-rotating crescent like flow are observed on both sides of the cylinder.

According to the classification of Tatsuno and Bearman [14], Figure 8(a) belongs to regime E and is three dimensional in form. The two-dimensional flow calculation at $Re=210.0$, $\mathrm{KC}=6.0$ is illustrated in Figures 8(b) and 8(c) and they suggest that the three-dimensional flow feature is not too strong although a slightly sharper V fluid shedding formation is shown in the simulation. This is a regime where the flow sheds with temporarily stable V-type vortex streets as illustrated in Figures 8(b), 8(c) and 9(c). In this regime intermittent changes of direction of convection and switching of the flow field triggered by small disturbances were observed by Tatsuno and Bearman [14]. However, no artificial disturbances (e.g. see the discussion of Zhang and Zhang [21]) were added in the present computations to simulate

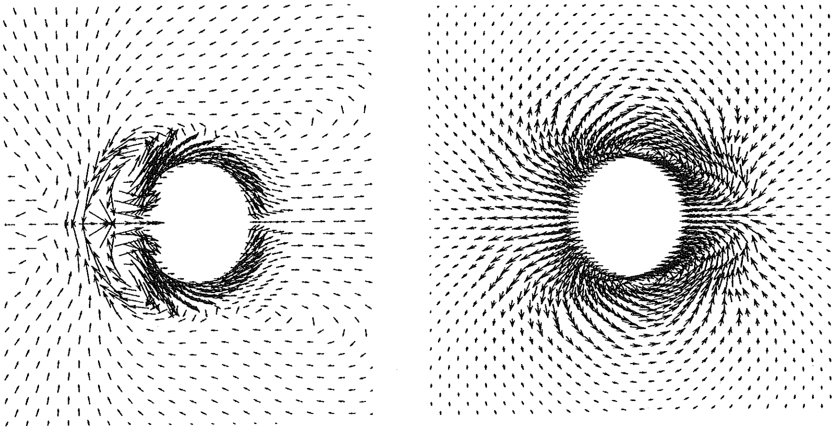

(a) Re=81.4, KC=11.0, Ut/D = 250.21

(b) Re=165.79, KC=3.14, Ut/D = 59.64

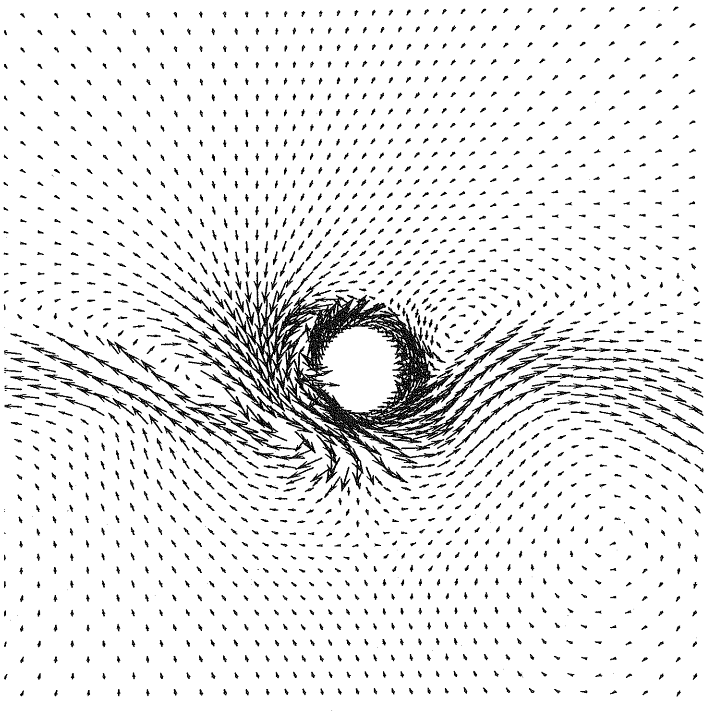

(c) Re=210.0, KC=6.0, Ut/D = 465.00

Figure 9. An enlargement of the velocity field at a presented instant in the vicinity of the transversely oscillating cylinder for the flow regimes illustrated in Figures 6(c)–8(c).

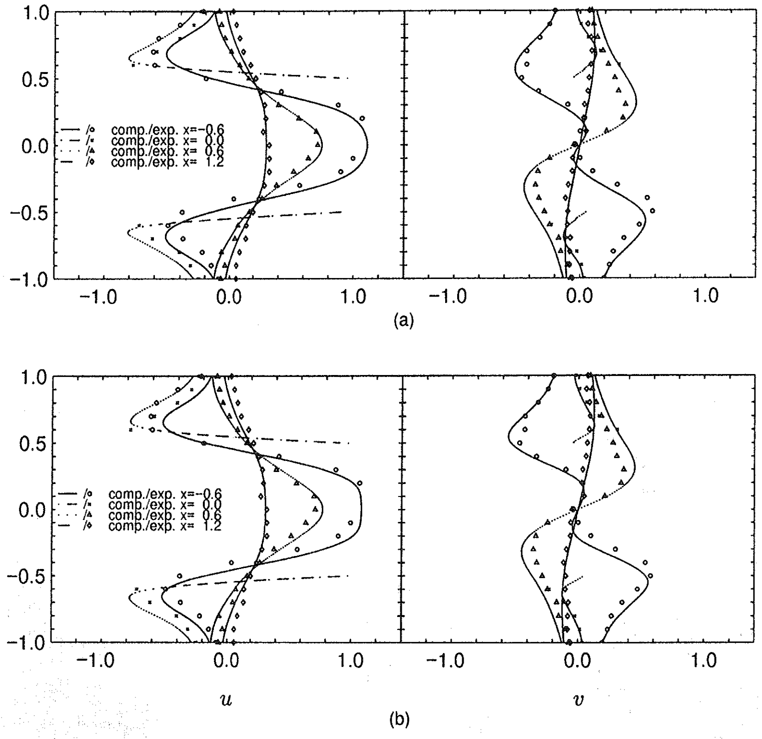

Figure 10. Comparison of the velocity components at four cross-sections at constant x values of $\alpha_1, \alpha_2, \alpha_3, \alpha_4$ as illustrated in Figure 4. These results relate to a phase position 180° computed by discretization utilizing (a) a coarse mesh (see Table III, row 1); (b) a medium mesh (see Table III, row 2).

this mechanism and vorticity convection occurred only on one side of the cylinder with no switching of the flow field.

To further validate the proposed theoretical and numerical approach, computations were compared with measurements taken by Dütsch *et al.* [15] at $Re = 100$ and $\mathrm{KC} = 5.0$ for the velocity components (u, v) at prescribed phase angles and at different cross-sections in the flow measured from the centre of the cylinder. Figure 4 indicates the four transverse positions of measurement $\alpha_1, \alpha_2, \alpha_3, \alpha_4$. Figure 10 illustrates such a comparison at these cross-sections behind and ahead of the cylinder. The excellent comparison between these findings and the experimental and numerical results of Dütsch *et al.* [15] further confirms with confidence the applicability of the mathematical model to fluid–structure interaction problems defined by low Reynolds number and Keulegan–Carpenter number.

4.3. Predicted forces and coefficients

To illustrate the influence of Reynolds number and Keulegan–Carpenter number on force and coefficient values a series of computations were undertaken along the $\beta = 35$ line shown in Figure 1 for $0 \leqslant \mathrm{KC} \leqslant 8$. This range covers two- and three-dimensional flow regimes and therefore, for KC values greater than approximately 5 along $\beta = 35$ the predicted values can

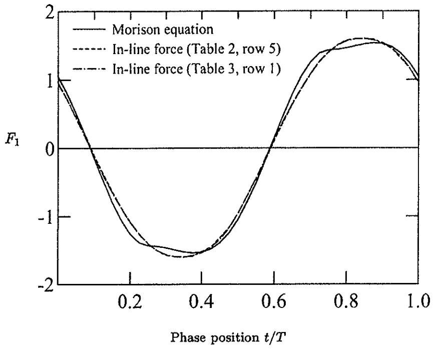

Figure 11. In-line force computed over a cycle at $Re = 100$ and KC = 5. (Note that the computed results associated with --- and -·- coincide.)

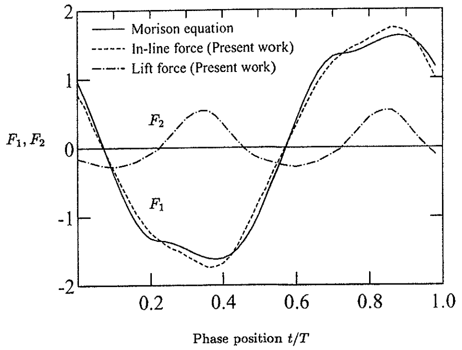

Figure 12. In-line and lift forces computed over a cycle at $Re = 210$ and KC = 6.

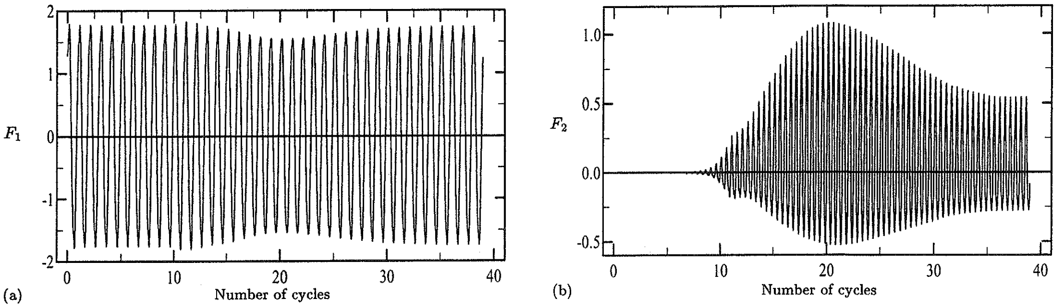

Figure 13. Time history of (a) in-line force and (b) lift force computed at $Re = 210$ and KC = 6.

only be approximations to the physical flow reality. As indicated in the introduction, the KC parameter in effect compares the distance the cylinder moves relative to the cylinder's diameter. When the KC value is small inertial forces dominate, the time for diffusion of vorticity is insufficient and the flow remains attached. With increasing value of KC, the boundary layer separates, vortex formation and shedding occurs and drag forces become important. Vorticity is now transported by convection as well as diffusion as discussed by Kühtz [32].

For illustration purposes, Figures 11 and 12 show the variation of the drag (F_1) and lift (F_2) force components over a cycle at $Re = 100$, KC = 5 and $Re = 210$, KC = 6, respectively. The information is computed directly by the cell boundary element method and through analysis using the Morison equation (3) after determining C_D and C_I values by Fourier analysis. As to be expected, a reasonable agreement exists between the drag force component from the two analyses. The individually calculated time force histories of the components illustrated in Figure 12 are shown in Figures 13(a) and 13(b). The initially zero-valued lift force component indicates a symmetric flow field before the presence of the lift force is experienced which significantly lags the drag force. For the two-dimensional flow regime at $Re = 100$, KC = 5 the lift force component F_2 remains zero or very near to zero over the cycle confirming a

Table IV. Drag C_D and added mass C_I coefficients for $\beta = 35$ at different regimes.

KC Regime	0.5 A*	1.0 A*	1.5 A*	2.0 A*	2.5 A*	3.0 A*	4.0 A	5.0 C	6.0 E	8.0 F†
					Viscous cell boundary element method					
C_D	10.0	5.13	3.56	2.83	2.43	2.18	1.94	1.84	1.75	1.74
C_I	1.37	1.36	1.35	1.33	1.32	1.30	1.29	1.23	1.14	1.05
					Finite volume method, Dütsch et al. [15]					
C_D	10.4	5.39	3.72	2.98	—	2.28	1.97	1.82	1.73	1.72 – 1.73
C_I	1.37	1.36	1.35	1.34	—	1.31	1.30	1.30	1.17	1.14 – 1.15

†Cycle averaged after flow instability.

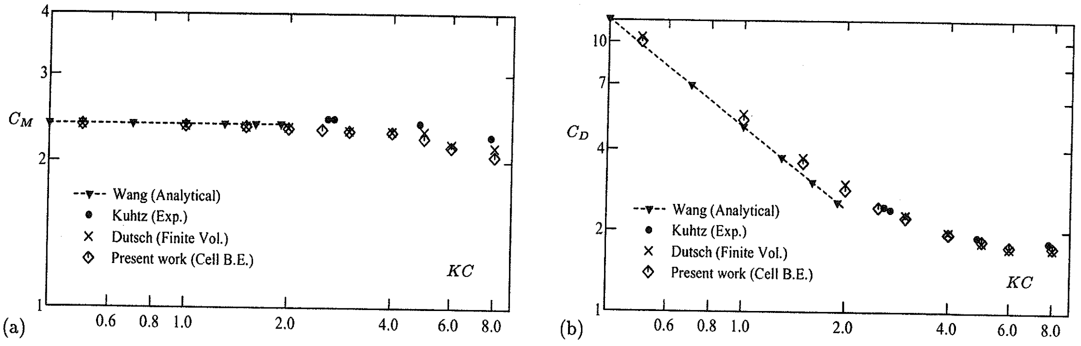

Figure 14. Variation of (a) inertia coeffcient C_M and (b) drag coefficient C_D with Keulegan–Carpenter number KC for $\beta = 35$.

symmetric flow field and the drag force is the only significant component. In both cases a reasonable correlation exists between the Morison type approach and results derived from the cell boundary element approach.

Table IV presents information on the drag C_D and added mass C_I coefficients from the series of computations over KC number. These coefficients for $\mathrm{KC} \geqslant 5$ were obtained by Fourier analysis of the cycles after periodic states were established. This table also includes a comparison with the findings of Dütsch *et al.* [15] for $0 \leqslant \mathrm{KC} \leqslant 8$, $\beta = 35$ using a finite volume method. In flow region F $(\mathrm{KC} = 8.0)$ a time-averaging process is applied to the cyclical data after the occurrence of flow instability. All these data are included in Figures 14(a) and 14(b) together with the experimental results of Kühtz [32], who presented the data in this inertia-drag coefficient format and analytical solutions of Wang [25] derived from (5) and (6). From this limited evidence, the agreement between experimental drag data and cell boundary element method or finite volume method predictions are favourable although for the added inertia coefficient the predicted values lie below the experimental data. Furthermore, the information illustrates the restricted accuracy of the series expansion as performed by Wang and confirms the limited applicability of such an approach as discussed by Chester [41].

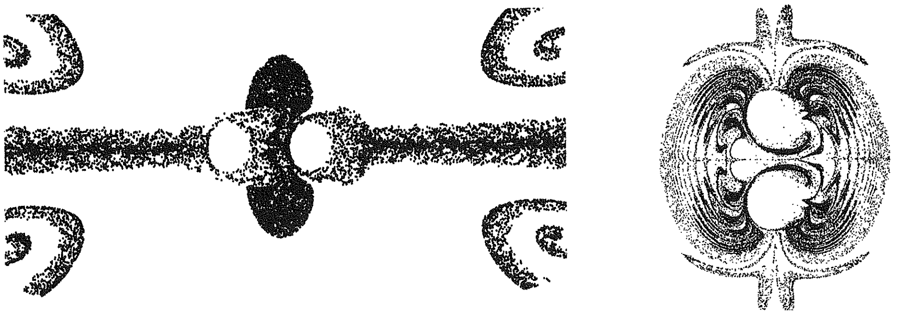
(a) (b)

Figure 15. The simulated streakline patterns generated by two oscillating circular cylinders at $Re = 100$, KC = 5 in (a) tandem arrangement and (b) side-by-side arrangement. The gap clearance between the two cylinders is D in both cases where D is the diameter of the cylinders.

Table V. Key parameters for two oscillating cylinders at $Re = 100$ and KC = 5.

Parameters	Single cylinder	Two cylinders in tandem		Two cylinders side-by-side	
		Left	Right	Bottom	Top
C_D	2.10	1.77	1.77	2.63	2.63
C_I	1.43	1.25	1.25	1.30	1.30
$\bar{F}_1$	0.0	−0.10	0.10	0.0	0.0
$\bar{F}_2$	0.0	0.0	0.0	0.30	−0.30

4.4. *Two oscillating cylinders*

The cell boundary element method has also been used in multi-body problems and the application is straightforward since this method works with unstructured meshes. Examples presented here involve two identical cylinders oscillating in synchronization with parameters $Re = 100$ and KC = 5 based on the diameter D of the cylinders. Two arrangements with the cylinders in tandem and side by side are considered and in both cases the gap between the two cylinders is the same as the diameter of the cylinders. That is, the distance from centre to centre of the cylinders is $2D$. The simulated streakline patterns predicted using the cell boundary element method are presented in Figure 15 ((a) for the tandem arrangement and (b) for the side-by-side arrangement). As can be seen in Figure 15, the streakline pattern of the tandem arrangement appears to be similar to the single cylinder case in the same regime whereas the side-by-side arrangement produces a very different streakline pattern.

The drag C_D and added mass C_I coefficients and time averaged values of in-line force $\bar{F}_1$ and lift $\bar{F}_2$ are shown in Table V for each cylinder in different arrangements. The C_I values in both the two cylinder cases are lower for each arrangement when compared with the C_I value of a single cylinder, whereas the C_D values show a different trend. The values of $\bar{F}_1$ and $\bar{F}_2$ in Table V suggest that the two cylinders are subject to a net repulsive force in the tandem arrangement and a net attractive force in the side-by-side arrangement. The results also show that the interactions between the two cylinders are significant in both arrangements under the given conditions.

5. CONCLUSION

The cell boundary element method developed by Tan *et al.* [29] and modified herein to study oscillating cylinders or manoeuvring bodies has proven successful, reproducing the detailed characteristics of experimental observations, correlations with theoretical predictions presented by others and experimental measurements of drag and lift coefficients over a range of Re, KC numbers for fixed Stokes' parameter $\beta = 35$. This has been achieved by adopting an unstructured mesh to idealize the fluid domain and a primitive-variable formulation to construct a hybrid approach involving boundary element and finite element methods. Through developments of suitable numerical schemes of study associated with the cell boundary element method integrated with the relevant boundary conditions for transversely oscillating cylinders or a cylinder fixed in oscillating flows, the presented computed unsteady flows provide a measure of verification, validation and confidence in the proposed overall approach when compared with other experimental and theoretical findings.

ACKNOWLEDGEMENTS

We gratefully acknowledge the experimental data supplied by Dr. Stefan Becker from the study undertaken by Dütsch, Durst, Becker and Lienhart.

REFERENCES

1. Duncan WJ. *The Principles of the Control and Stability of Aircraft.* Cambridge University Press: Cambridge, 1959.
2. Burcher RK. Developments in ship manoeuvrability. *Transactions of the Royal Institution of Naval Architects* 1972; **114**:1–32.
3. Etkin B. *Dynamics of Atmospheric Flight.* Wiley: New York, 1972.
4. Sarpkaya T, Isaacson M. *Mechanics of Wave Forces on Offshore Structures.* Van Nostrand Reinhold: New York, 1981.
5. Faltinsen MO. *Sea Loads on Ships and Offshore Structures.* Cambridge University Press: Cambridge, 1990.
6. Baltrop NDP, Adams AJ. *Dynamics of Fixed Marine Structures.* Butterworth-Heinemann: London, 1991.
7. Hassan AY. The effects of vibration on the lift and drag forces on a circular cylinder in a fluid flow. *Ph.D. Thesis*, University College London, University of London, 1962.
8. Bishop RED, Hassan AY. The lift and drag forces on a circular cylinder in a flowing fluid. *Proceedings of the Royal Society of London A* 1964; **277**:51–75.
9. Maull DJ, Milliner MG. Sinusoidal flow past a circular cylinder. *Coastal Engineering* 1978; **2**:149–168.
10. Bearman PW, Downie MJ, Graham JMR, Obasaju ED. Forces on cylinders in viscous oscillatory flows at low Keulegan–Carpenter numbers. *Journal of Fluid Mechanics* 1985; **154**:337–352.
11. Williamson CHK. Sinusoidal flow relative to circular cylinders. *Journal of Fluid Mechanics* 1985; **155**:141–174.
12. Williamson CHK. 2-D and 3-D aspects of the wake of a cylinder, and their relation to wake computations. *Lectures in Applied Mathematics* 1991; **28**:719–751.
13. Obasaju ED, Bearman PW, Graham JMR. A study of forces, circulation and vortex around a circular cylinder in oscillating flow. *Journal of Fluid Mechanics* 1988; **196**:467–494.
14. Tatsuno M, Bearman PW. A visual study of the flow around an oscillating circular cylinder at low Keulegan–Carpenter numbers and low Stokes numbers. *Journal of Fluid Mechanics* 1990; **211**:157–182.
15. Dütsch H, Durst F, Becker S, Lienhart H. Low-Reynolds-number flow around an oscillating circular cylinder at low Keulegan–Carpenter numbers. *Journal of Fluid Mechanics* 1998; **360**:249–271.
16. Borthwick A. Comparison between two finite-difference schemes for computing the flow around a cylinder. *International Journal for Numerical Methods in Fluids* 1986; **6**:275–290.
17. Smith PA, Stansby PK. Viscous oscillatory flow around cylindrical bodies at low Keulegan–Carpenter numbers using vortex methods. *Journal of Fluids Structures* 1991; **5**:339–361.
18. Justesen P. A numerical study of oscillating flow around a circular cylinder. *Journal of Fluid Mechanics* 1991; **222**:157–196.
19. Wang CY, Dalton C. Oscillating flow past a rigid circular cylinder: a finite difference calculation. *Transactions of ASME Journal: Journal of Fluids Engineering* 1991; **113**:377–383.

20. Lin XW, Bearman PW, Graham JMR. A numerical study of oscillatory flow about a circular cylinder for low values of beta parameters. *Journal of Fluids Structures* 1996; **10**:501–526.
21. Zhang HL, Zhang X. Flow structure analysis around an oscillating circular cylinder at low *KC* number: a numerical study. *Computers and Fluids* 1997; **26**:83–106.
22. Morison JR, O'Brien MP, Johnson JM, Schaaf SA. The force exerted by surface waves on piles. *Petroleum Transactions of AIME* 1950; **189**:149–154.
23. Sarpkaya T. Vortex shedding and resistance in harmonic flow about smooth and rough cylinders at high Reynolds number. *Report No. NPS*-59SL76021, Naval Postgraduate School, Monterey, California, USA, 1976.
24. Stokes GG. On the effect of the internal friction of fluids on the motion of pendulum. *Transactions of Cambridge Philosophical Society* 1852; **9**:8–106.
25. Wang CY. On high-frequency oscillatory viscous flows. *Journal of Fluid Mechanics* 1968; **32**:55–68.
26. Honji H. Streaked flow around an oscillating cylinder. *Journal of Fluid Mechanics* 1981; **107**:509–520.
27. Hall P. On the stability of the unsteady boundary layer on a cylinder oscillating transversely in a viscous fluid. *Journal of Fluid Mechanics* 1984; **146**:347–367.
28. Sarpkaya T. Force on a circular cylinder in viscous oscillatory flows at low Keulegan–Carpenter numbers. *Journal of Fluid Mechanics* 1986; **165**:61–71.
29. Tan M, Farrant T, Price WG. A cell boundary element method for viscous laminar flow solutions. *Proceedings of the Royal Society of London A* 1999; **455**:4277–4304.
30. Farrant T, Tan M, Price WG. A cell boundary element method applied to laminar vortex shedding from circular cylinders. *Computers and Fluids* 2001; **30**(2):211–236.
31. Farrant T, Tan M, Price WG. A cell boundary element method applied to laminar vortex shedding from arrays of cylinders in various arrangements. *Journal of Fluids Structures* 2000; **14**(3):375–402.
32. Kühtz S. Experimental investigation of oscillatory flow around circular cylinders at low beta numbers. *Ph.D. Thesis*, University of London, 1996.
33. Price WG, Tan M. Fundamental viscous solutions or 'transient oseenlets' associated with a body manoeuvring in a viscous fluid. *Proceedings of the Royal Society of London A* 1992; **438**:447–466.
34. Stiefel EL. *An Introduction to Numerical Mathematics*. Academic Press: New York, 1963.
35. Tan M. A Viscous boundary element approach to fluid flow-structure interaction problems. *Ph.D. Thesis*, University of Southampton, 1994.
36. Price WG, Tan M. The evaluation of steady fluid forces on single and multiple bodies in low speed flows using viscous boundary elements. In *Proceedings of International Conference on the Dynamics of Marine Vehicles and Structures in Waves, 1990*, Price WG, Temarel P, Keane AJ (eds). Elsevier: Amsterdam, 1992; 125–133.
37. Press WH, Flannery BP, Teukolsky SA, Vetterling WT. *Numerical Recipes*. Cambridge University Press: Cambridge, 1986.
38. Zienkiewicz OC. *The Finite Element Method*. McGraw-Hill: New York, 1977.
39. Garrison CJ. Drag and inertia forces on a cylinder in harmonic flow. *Journal of Waterway, Port, Coastal and Ocean Engineering* ASCE 1990; **103**(WW2):169–190.
40. Knörnschild U. Experimentelle Unterschungen der Stromungsverhaltnisse um einen oszillierenden Kreiszylinder. *Master's Thesis*, University of Erlangen-Nurnberg, LSTM, Erlangen, 1994.
41. Chester W. A general theory for the motion of a body through a fluid at low Reynolds number. *Proceedings of the Royal Society of London A* 1990; **430**:89–104.